

Multiwall carbon nanotube@mesoporous carbon with core-shell configuration: a well-designed composite-structure toward electrochemical capacitor application†

Xufang Qian, Yingying Lv, Wei Li, Yongyao Xia and Dongyuan Zhao*

Received 11th May 2011, Accepted 13th June 2011

DOI: 10.1039/c1jm12082d

Based on the desired electrical conductivity and high specific-surface-area for carbon-based electrodes, herein, we have designed and synthesized uniform multiwall carbon nanotube@mesoporous carbon (MWNT@mesoC) composites with core-shell configuration by combining sol-gel methods and nanocasting. Pristine MWNTs after acid treatment were first coated with uniform mesostructured silica shells to obtain the MWNT@mesoporous silica (MWNT@mesoS) composite using cationic surfactant cetyltrimethyl ammonium bromide (CTAB) as a template. Then, furfural alcohol (carbon source) and oxalic acid (catalyst) were impregnated into the template-free MWNT@mesoS composite and followed by carbonization. The removal of silica led to the replacement of the mesoC shells decorated on the surface of MWNTs. The obtained composite materials retain the one-dimension (1-D) tubular structure and three-dimension (3-D) entangled framework as the original MWNTs. Micro/nanostructure exploration demonstrates that each MWNT is uniformly coated by the mesoC shell with short-pore-length (~15 nm), which contributes above 300 m² g⁻¹ to specific surface areas purely from bimodal-mesopores (3.9/8.9 nm in diameter). The MWNT@mesoC composite shows greatly increased specific capacitance from 9.0 to 48.4 F g⁻¹ and 6.8 to 60.2 F g⁻¹ in 1.0 M (C₂H₅)₄NBF₄ and 6.0 M KOH, good rate performance with ~60% maintenance of the initial capacitance at the current density of 20 A g⁻¹ and high cyclability (94% after 1000 cycles).

Introduction

Recent attention in electrochemical capacitors (ECs) has focused on the development of carbon materials for high rate electric devices due to their available high surface area, good chemical and thermal stability as well as low cost.¹⁻⁷ Carbon nanotubes (CNTs) are now intensively studied as new electrode materials because of their unique 1-D tubular structure, high mechanical strength, and excellent electrical conductivity.⁸⁻¹¹ The capacitance performance of CNTs is tightly correlated with their intrinsic physicochemical properties, such as specific surface area and surface chemistry.⁸ Generally, the specific capacitance value

of CNTs in organic electrolyte is lower than 60 F g⁻¹, which depends on the different synthesis parameters and post-treatments.^{8,11} The low capacitance of CNTs is mainly caused by the limited surface area (typically less than 200 m² g⁻¹), closed tips and the hydrophobic surface.⁸ Recently, composite electrodes, namely CNTs modified with allotropic carbon nanohorns⁹ and aerogels¹² have been employed to increase the specific capacitance on the principle of electrical double layer capacitors (EDLC), which showed remarkable enhancement in EC performance.

Mesoporous carbons (MesoCs) with uniform and interconnected pore networks could facilitate the diffusion of ions to the surface, and therefore were considered as promising candidates for EC electrodes.^{6,13-15} Notably, it has been proven that the short-pore-length of mesoCs facilitates the dynamic process of inner-pore electric double layer formation.¹⁶ However, owing to its disordered amorphous nature of mesoC, its electrical conductivity is poor relative to graphite-based materials, which is significantly related to power performance.⁹ In order to improve the power density of supercapacitors, it is crucial to enhance the kinetics of ion and electron transport in electrodes and at the electrode/electrolyte interface.^{1,17,18} Thus, well-tailored composite configuration with high specific surface area and good electrical conductivity are highly desired for carbon-based

Department of Chemistry, Shanghai Key Laboratory of Molecular Catalysis and Innovative Materials, Laboratory of Advanced Materials, Fudan University, Shanghai, 200433, P. R. China. E-mail: dyzhao@fudan.edu.cn; Fax: +86-21-5163-0307; Tel: +86-21-5163-0205

† Electronic supplementary information (ESI) available: SEM image of the pristine MWNTs; FESEM images of MWNT@mesoC composites; TG/DTG curves of MWNTs and the mechanical mixture; CVs of the pristine MWNTs and MWNT@mesoC composites; CVs and rate performance of the mesoC; Cyclability of the pristine MWNTs, MWNT@mesoC composite and mesoC; CVs of the pristine MWNTs, MWNT@mesoC composite and mesoC in 6.0 M KOH electrolyte; Nyquist plots of the MWNT@mesoC composite and mesoC. See DOI: 10.1039/c1jm12082d

electrode materials. However, it is still a challenge to controllably construct mesoporous carbon shells on the inert and enormously curved surface of CNTs to obtain uniform CNTs/mesoporous carbon composites, which has promoted researchers to explore the correlations between composite configuration and EC performances.

Herein, we designed and synthesized MWNT@mesoC with a core-shell configuration by combining sol-gel coating pathways and nanocasting strategies (Scheme 1). MWNT@mesoS composite with a core-shell structure was primarily prepared and it served as a “hard template” which was soaked with furfural alcohol and oxalic acid. After carbonization, the subsequent silica removal led to the replacement of mesoC shells decorated on the surface of MWNTs. MWNT@mesoC composite shows initial 1-D tubular structure and 3-D entangled network. MesoC shells with a thickness of ~15 nm and uniform bimodal-pore sizes of ~3.9/8.9 nm are uniformly coated on the surface of MWNTs, contributing specific surface area of above 300 m² g⁻¹. The MWNT@mesoC composite with core-shell configuration shows improved EC performances relative to the pristine MWNTs and mesoC due to the effective transport of electrons and electrolyte ions in the composite structure.

Experimental

Chemicals and materials

Cetyltrimethyl ammonium bromide (CTAB, ≥99.0%), tetraethyl orthosilicate (TEOS, ≥98%), ethanol (≥99.7%), ammonia (28%), furfuryl alcohol (≥98.0%), oxalic acid (≥99.5%) and HF aqueous solution (≥40%) were purchased from Shanghai Chemical Corp. (Shanghai, China). All chemicals were used as received without further purification. Millipore water was used in all experiments.

Commercial MWNTs were purchased from Shenzhen Nanotech Port Co. Ltd. (Shenzhen, China). Prior to use, MWNTs were treated with concentrated acids (H₂SO₄/HNO₃ = 1/1 (v/v)) in the presence of ultrasonic for purification. The acid-treated

MWNTs were washed with copious of water and then dried at 60 °C.

Synthesis of MWNT@mesoS composites

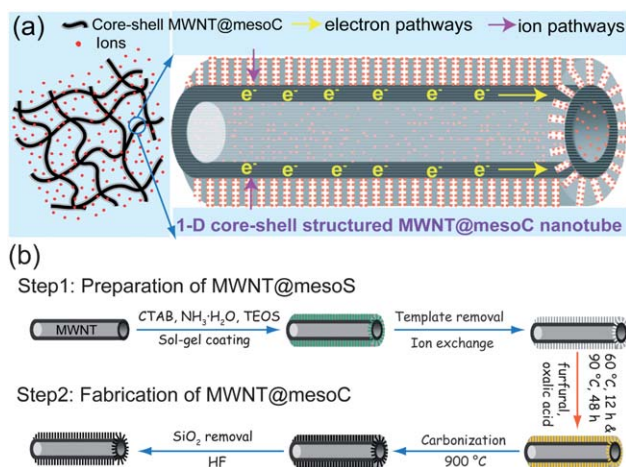
The coating of mesoporous silica on MWNTs was implemented according to a facile sol-gel coating pathway.¹⁹ In a typical synthesis, 0.16 g of CTAB was dissolved into a mixture solution containing 30 mL of deionized water, 120 mL of ethanol and 1.5 mL of ammonia (28 wt%) at room temperature (25 °C). Subsequently, 100 mg of MWNTs were dispersed into the above mixture under ultrasonic treatment for ~30 min to obtain a homogeneous mixture. Then, TEOS (0.94 g) was added and the reaction mixture was stirred for 6 h in absence of ultrasonic treatment. Finally, the obtained product was centrifuged and washed with ethanol and water. The surfactants were removed by ion exchange (2.0 g of NH₄NO₃ in 120 mL of ethanol) to obtain a template-free core-shell structured MWNT@mesoS composite material for further use.

Synthesis of MWNT@mesoC composites

MesoC shells were constructed on MWNTs by using MWNT@mesoS composite as a hard template, furfuryl alcohol as a carbon source and oxalic acid as a catalyst using a nanocasting strategy. Typically, an ethanol solution of furfuryl alcohol with oxalic acid was mixed homogeneously with MWNT@mesoS composites under hand stirring for 30 min. The weight ratios of hard template: furfuryl alcohol: oxalic acid was in the range of 1.0 : 1.0–1.8 : 0.01 determined by the total pore volume (*V_t*) of the hard template (MWNT@mesoS composite). Later, the furfuryl alcohol/hard template mixture was placed in a closed Teflon bottle, and then heated at 60 °C for 12 h and subsequently 90 °C for 48 h in order to completely fill the nanopores with carbon source. The furfuryl alcohol/MWNT@mesoS composites were pyrolyzed at 150 °C for 3 h and carbonized at 900 °C for 2 h to obtain the MWNT@mesoS/C composites. Heating rates were 1 °C min⁻¹ below 350 °C and 5 °C min⁻¹ between 350 and 900 °C, respectively. Subsequent silica etching in a HF aqueous solution (10%) gave rise to MWNT@mesoC composites with the carbon shells instead of silica shells. *Caution! Hydrofluoric acid (HF) is extremely corrosive. It should be used with extreme care.* Control sample, mesoporous carbon, was also prepared by the nanocasting method using CTAB-templated mesoporous silica (MesoS) as a nanomould, which was obtained in a similar reaction solution but without addition of MWNTs, in comparison with the preparation of MWNT@mesoS.

Characterization

Powder XRD patterns were recorded on a Bruker D8 diffractometer with Ni-filtered Cu-Kα radiation (40 mV, 40 mA, Bruker, Germany). Nitrogen sorption isotherms were measured at 77 K on a Quantachrome Autosorb-1-MP (Quantachrome, USA). Before measurements, all of the samples were degassed in vacuum at 300 °C for at least 10 h. The Brunauer–Emmett–Teller (BET) method was used to calculate the specific surface areas (*S_{BET}*) using adsorption data in a relative pressure range from 0.05 to 0.3. The pore size distributions (PSD) were obtained by



Scheme 1 Well-designed MWNT@mesoC composites with core-shell configuration toward EC electrode application (a), and schematic representation of the synthesis route to MWNTs@mesoC composites by combining sol-gel coating pathway and nanocasting strategy (b).

applying the equilibrium model of non-local density functional theory (NLDFT method) for cylinder pore geometry. The total pore volume V_t was estimated from the adsorbed amount at a relative pressure p/p_0 of 0.995. The micropore volume (V_m) and micropore surface area (S_{micro}) were calculated from the V_t plot method. Transmission electron microscopy (TEM) images were recorded on a JEOL JEM-2100 F microscope (JEOL, Japan) operated at 200 kV. The samples for TEM measurements were dispersed directly in ethanol and collected using copper grids. Field-emission scanning electron microscope (FESEM) measurements were performed on a Hitachi S-4800 microscope (Hitachi, Japan). Au was coated on the materials on a MSP-1S sputter coater (Shinku VD, Japan) before being introduced into the electron microscope. TEM measurements were dispersed directly in ethanol and then collected using copper grids. SEM images were taken with a Philip XL30 microscope (Philip, Holland) operating at 20 kV. Raman spectra were collected on a Renishaw inVia Reflex microscopic Raman spectrometer (Renishaw, UK), using a He-Ne laser with an excitation wave length of 633 nm. Thermogravimetric (TG) analysis was conducted on a Mettler Toledo TGA-SDTA851 analyzer (Mettler Toledo, Switzerland) from 30 to 900 °C under air with a heating rate of 10 °C min⁻¹.

Electrochemical measurements

The electrode was prepared by mixing 90 wt% carbon material and 10 wt% poly(tetrafluoroethylene) (PTFE) binder dispersed in isopropanol. Electrochemical performance of different electrode materials were measured in both organic and aqueous electrolytes. For organic electrolyte, the slurries were coated on the metal foil (Al foil was employed as the current collector). After coating, the electrodes were dried at 80 °C for 10 min to remove the solvent before being pressed. The electrodes were vacuum-dried at 100 °C for 24 h, and weighed. The typical mass load was about 5 mg cm⁻². The electrochemical measurements were performed using electrochemical analyzer, CHI760. The electrolyte was 1.0 M (C₂H₅)₄NBF₄ in propylene carbonate (PC) (Honeywell Corp). The voltage range for CV and galvanostatic charge-discharge varies from 0.0 V to 3.0 V. The current density for the galvanostatic measurement varied from 0.5 to 20 A g⁻¹. For aqueous electrolyte, the slurries were pressed onto the Ni foam current collector and then dried at 120 °C for 12 h to remove the solvent and water. The experiments were carried out using a three-electrode cell, in which platinum and Hg/HgO electrodes (in 6.0 M KOH) were used as counter and reference electrodes, respectively. The electrochemical behaviors of the MWNT@mesoC and mesoC electrode materials were measured by cyclic voltammetry (CV) and electrochemical impedance spectroscopy (EIS) analysis (Solartron Instrument Model 1287 electrochemical interface and 1255B frequency response analyzer controlled by a computer).

Results and discussions

A composite configuration comprising of MWNT as the inner core and mesoC as the outer shell was designed (Scheme 1a). The MWNT@mesoC composites with core-shell configuration were synthesized by combining sol-gel coating with nanocasting

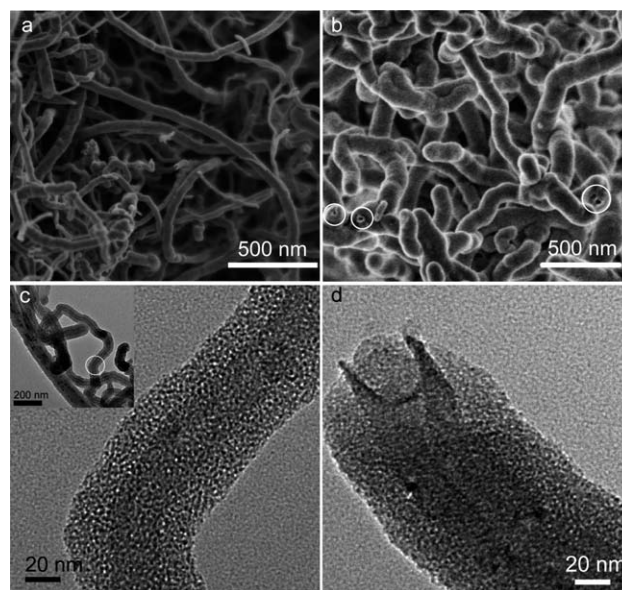


Fig. 1 FESEM and TEM images: (a) the pristine MWNTs with outer diameter and length in the range of 40–100 nm and 5–15 μm , respectively; (b–d) the MWNT@mesoS composite prepared by a sol-gel coating pathway using CTAB as a template showing uniform core-shell structure with shell thickness of ~ 20 nm and interpenetrated mesoporous networks.

strategy (Scheme 1b). The outer diameter and the length of the pristine MWNTs are in the range of 40–100 nm and 5–15 μm (product data from Shenzhen Nanotech Port Co. Ltd), which entangle with each other to form a 3-D network (Fig. 1a). The FESEM image shows the smooth surface (Fig. S1, ESI[†]). After sol-gel coating, each nanotube (Fig. 1b) is obviously thicker than that of the pristine MWNT. The mesostructured silica shells with ~ 20 nm thickness can be clearly observed from the cross section of MWNT@mesoS composite-nanotubes (white circles in Fig. 1b). These results indicate the successful and exclusive coating at the MWNT-liquid interface without impurity. The TEM image (inset of Fig. 1c) also confirms that the mesoS shells ~ 20 nm thick are uniformly coated around the sidewall of MWNTs. High resolution TEM (HRTEM) images are clearly visible (Fig. 1c,d) showing that the curved and interpenetrated mesopore channels are toward the surface of MWNTs, and the junction between the MWNTs and silica shells is very compact. By using this composite material as a nano-mould, a core-shell structured MWNT@mesoC composite with mesoporous carbon shells instead of silica shells can be produced.

As shown in Fig. 2a, uniform 1-D tubular structures with the retained morphology as the original MWNT are observed without separated particles and naked MWNTs, and the surface seems coarser than those of the pristine MWNTs. High-resolution FESEM image (HRFESEM) (Fig. 2b) shows plenty of opened mesopores of size of around 3.0 nm on the MWNT@mesoC composites. Moreover, a small quantity of MWNT@mesoC composites (Fig. S2a, ESI[†]) shows crumpled mesoC shells in addition to a majority of composite nanotubes with even shells (Fig. 2a and Fig. S2b, ESI[†]), implying that the presence of few incompact junctions of the core-shell configuration are unable to support the carbon shell. The TEM image

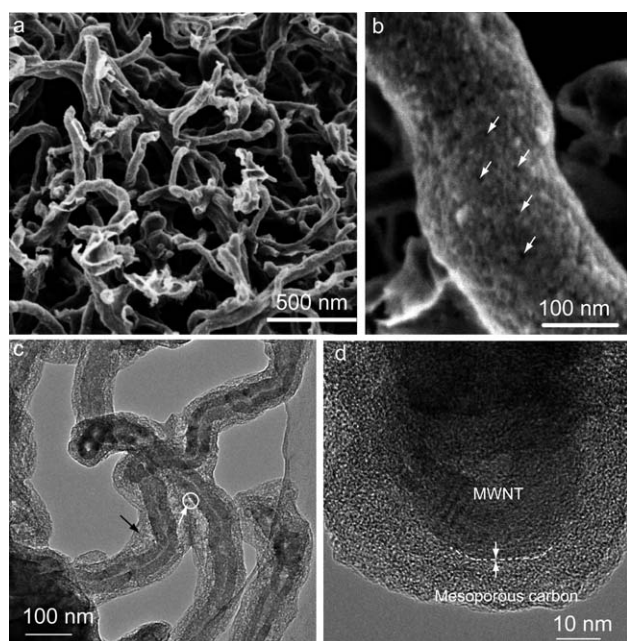


Fig. 2 FESEM and TEM images of the MWNT@mesoC composite: (a) FESEM image showing unchanged 1-D tubular structures entangled to a 3-D network; (b) HRFESEM image clearly showing rough surface after mesoC shell decoration and plenty of observable mesopores (~ 3.0 nm); (c) TEM image demonstrating uniform core-shell configuration with shell-thickness of ~ 15 nm and some defective domains (white circle); (d) HRTEM image showing the compact junction between the graphite layers of the MWNT and the amorphous mesoC shell.

demonstrates that the mesoC shells with thickness of ~ 15 nm uniformly grow around the MWNTs, indicating the perfect replication from silica to carbon and the short-pore-length characteristic of mesoC shell (Fig. 2c). Compared with that of the MWNT@mesoS composite, the shell thickness of the nanocasted MWNT@mesoC decreases from ~ 20 to 15 nm, basically resulting from the framework shrinkage during the carbonization at 900°C . The cross-section TEM image of the MWNT@mesoC composite nanotube (Fig. 2d) shows that the amorphous and continuous carbon shell with disordered mesostructure tightly connects with the graphite layers of MWNTs. Notably, the domain in the white circle (Fig. 2c) shows loose junction between the carbon shell and MWNT core, which probably results from the crumpled carbon shell. These phenomena suggest that furfural alcohols are successfully filling the nanopores of the silica shells through a facile nanocasting strategy. However, the mesopore channels of the silica shell are not as perfect as those of SBA-15 (cylinder pores connected with mesotunnels),²⁰ which causes some “blind areas” inaccessible for furfural alcohols or with insufficient carbon source to sustain the compact junctions between the MWNT and carbon shell, and thus the loose junctions and crumpled carbon shells appear.

Pristine MWNTs (Fig. 3A(a)) show weak ability for N_2 adsorption at low and middle relative p/p_0 , but an upward volume adsorbed at p/p_0 above 0.9, which induces a low BET specific surface area (S_{BET} : $71\text{ m}^2\text{ g}^{-1}$), and a relatively large total pore volume (V_t : $0.33\text{ cm}^3\text{ g}^{-1}$) (Table S1, ESI†) attributed to the accessible central canals with diameter above 40 nm (Fig. 3B(a)). After the decoration with mesoS shells, the N_2 sorption

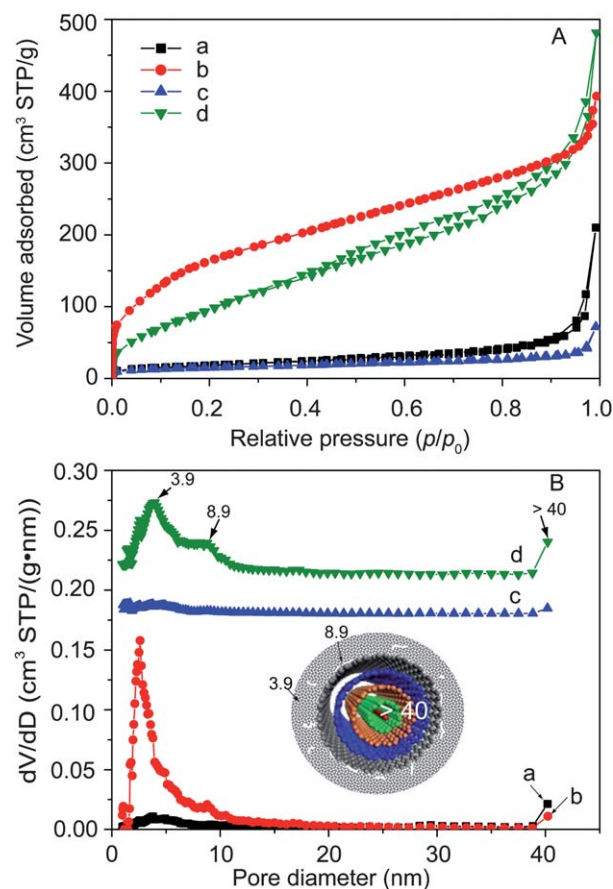


Fig. 3 Nitrogen sorption isotherms (A) and pore size distribution curves (B) of (a) the pristine MWNTs, (b) MWNT@mesoS, (c) MWNT@mesoC composite prior to silica etching, and (d) MWNT@mesoC composite. The pore size distributions for samples (c) and (d) were offset vertically by 0.18 and $0.22\text{ cm}^3\text{ g}^{-1}$.

isotherms (Fig. 3A(b)) demonstrate typical type-IV curves with an obvious capillary condensation step and a less obvious increase of N_2 volume adsorbed at high p/p_0 , indicating the hierarchical micro/mesopore characteristic of the silica shells and more or less closure of central canals in MWNTs due to mesoS coating. The S_{BET} increases to be $606\text{ m}^2\text{ g}^{-1}$ for the MWNT@mesoS, wherein 427 ($\sim 70\%$) and $179\text{ m}^2\text{ g}^{-1}$ ($\sim 30\%$) stem from the micropores and mesopores, respectively, and the V_t is $0.61\text{ cm}^3\text{ g}^{-1}$ (Table S1, ESI†). Combining with the previous TEM results, the textural properties of MWNT@mesoS reflect that the mesoS shells have interpenetrated pore networks in terms of curved channels interconnected with plenty of micropores, which facilitates the formation of a continuous mesoC shell rather than separated carbon nanorods.²¹ When MWNT@mesoS serves as a hard template and soaks with furfural alcohol to obtain the MWNT@mesoS/carbon (MWNT@mesoSC) composite after carbonization, the capillary condensation phenomenon of which (Fig. 3A(c)) disappears, and the V_t decreases to be $0.12\text{ cm}^3\text{ g}^{-1}$ suppressed by nearly 5 times relative to its mother hard template, indicating successful nanocasting. The MWNT@mesoC composite with core-shell configuration (Fig. 3A(d)) shows type-IV isotherms with a gentle capillary condensation step at $p/p_0 = 0.4\text{--}0.9$, corresponding to

uniform mesopores centered at the mean value of 3.9 and 8.9 nm (Fig. 3B(d)), which come from the voids of the silica wall removal and defect domains, respectively. The S_{BET} is calculated to be $381 \text{ m}^2 \text{ g}^{-1}$, which is totally from mesopores (Table S1, ESI†). The total pore volume is as high as $0.75 \text{ cm}^3 \text{ g}^{-1}$ due to the construction of mesoC and opened central canals.

Pristine MWNTs and core-shell structured MWNT@mesoC composite (Fig. 4A) exhibit similar wide-angle XRD patterns with one sharp and two weak diffraction peaks corresponding to the 002, 101 and 004 reflections, respectively, which suggests the typical characteristic of graphitic layers of MWNTs.²² The decreased intensity of diffraction peaks for the MWNT@mesoC composite relative to the pristine MWNTs is caused by the shield effect of the carbon shells to X-rays. Raman spectra of the pristine MWNTs before and after coating with the amorphous mesoC shells (Fig. 4B) show two characteristic peaks located at around 1565 (G-band) and 1355 cm^{-1} (D-band), which correspond to the C–C sp^2 interaction (E_{2g}) and the structural disorder in graphite material, respectively.^{23,24} The decreased band intensities after the coverage of the mesoC shell are caused by the shield effect of amorphous carbon shells. Additionally, the relative peak intensity ratio of the D-band to G-band for the pristine MWNTs is 0.62, but that of the MWNT@mesoC composite increases to 0.72, indicating the improved D-band relative intensity due to the presence of amorphous carbon shells.

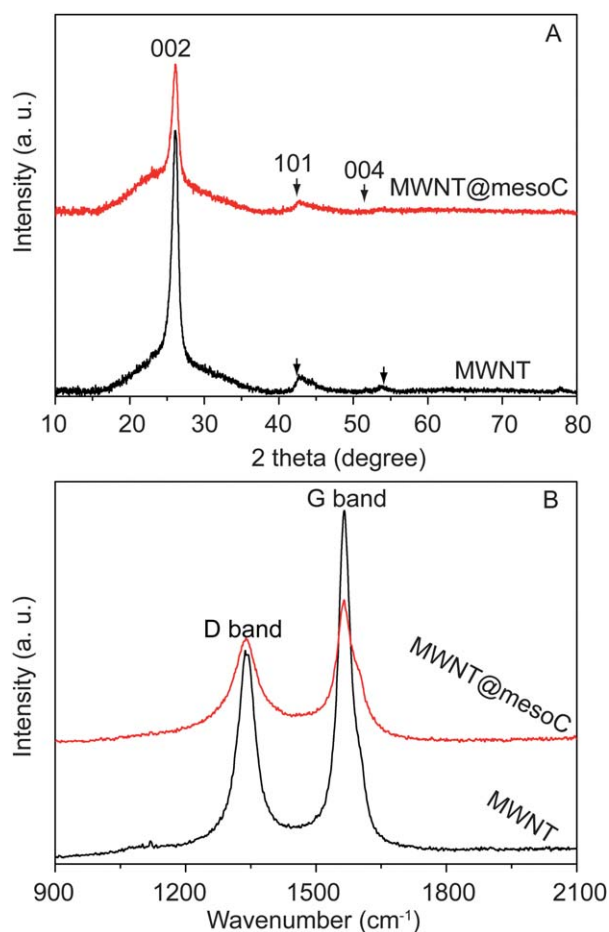


Fig. 4 Wide-angle XRD patterns (A) and Raman spectra (B) of the pristine MWNTs and MWNT@mesoC composite.

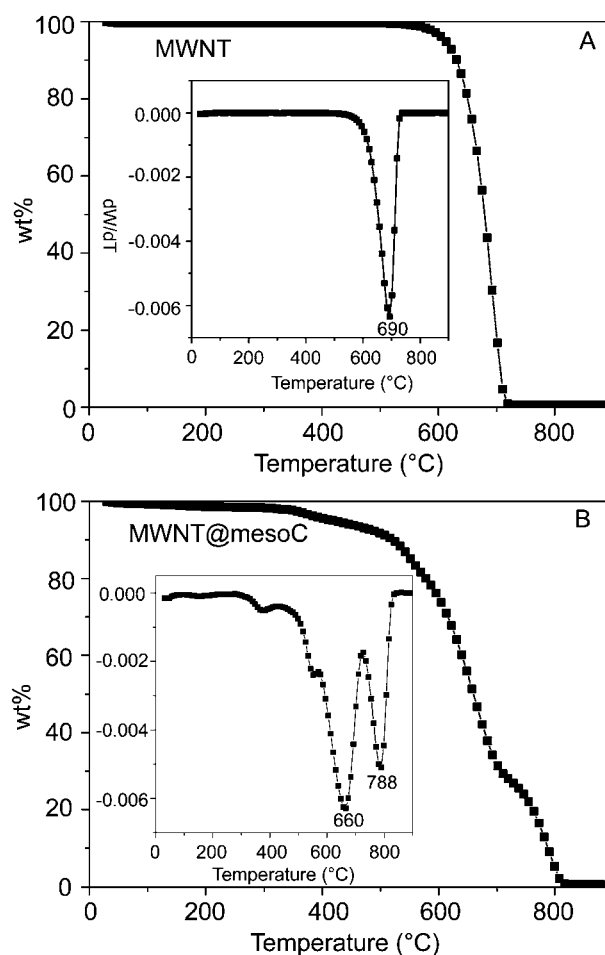


Fig. 5 TG and DTG (inset) curves of (A) the pristine MWNTs, and (B) MWNT@mesoC composite conducted in air from 30 to 900 °C.

TG analyses were employed to investigate the effect of mesoC shell upon the thermal behavior of MWNTs in air. Pristine MWNTs (Fig. 5A) shows negligible weight change before 550 °C, and then a dramatic weight loss from 550 to 710 °C in air. The corresponding differential TG (DTG) curve (inset of Fig. 5A) possesses a symmetric peak at 690 °C. The above phenomenon suggests the combustion process occurs only in one step, probably associated with the pure graphite composition, which is also reflected by the level TG curves of pristine MWNTs from 30 to 900 °C in N_2 (Fig. S3a, ESI†). The core-shell structured MWNT@mesoC composites display two obvious weight loss steps from 550 to 710 °C (Fig. 5B) corresponding to the two peaks in its DTG curve at 660 and 788 °C (inset of Fig. 5B), assigning to the decomposition of amorphous carbon component and inner MWNT cores, respectively. Interestingly, the presence of the mesoC shells result in combustion delay of nearly 100 °C relative to the pristine MWNTs, which reflects that the enhanced thermal stability of MWNTs by the protection of mesoC shells, and also implies the core-shell structured composite rather than the mechanical mixture (without combustion retard phenomenon in TG/DTG curves, Fig. S3b, ESI†).

The synthesis of the well-designed MWNT@mesoC composites with core-shell configuration is realized by combining a facile sol-gel method with nanocasting strategy. Hydrophobic

MWNTs treated with the acid mixture can be well-dispersed in ethanol and water solution, and then interact with CTAB at the solid-liquid interface to undergo the sol-gel coating process in basic medium with the addition of TEOS. Herein, the CTAB is directly incorporated in the Stöber synthesis solution with a high ethanol concentration, which tends to the formation of mesostructured silica shell with short-range ordered hexagonal symmetry and plenty of micropores, namely a more interpenetrated pore frameworks than ordered MCM-41 with long-range cylinder pores.²⁵ Based on the above structural data and the literature,²⁶ mesostructured silica coating basically occurs around the outer surface of CNTs, which is probably related to the higher energy required for the coating process in the interior surface relative to the outer sidewalls of CNTs.²⁷ By using this MWNT@mesoS composite as a nano-mould, small-molecule furfuryl alcohol can easily enter into the overall mesoS shells including the voids within the interfacial junction, which is responsible for the formation of the uniform MWNT@mesoC composites with integrated carbon shells and compact junctions. However, the existence of “blind areas” in the interpenetrated pore network of mesoS shells inevitable causes few crumpled but still continuous MWNT@mesoC composites after carbon replicating.

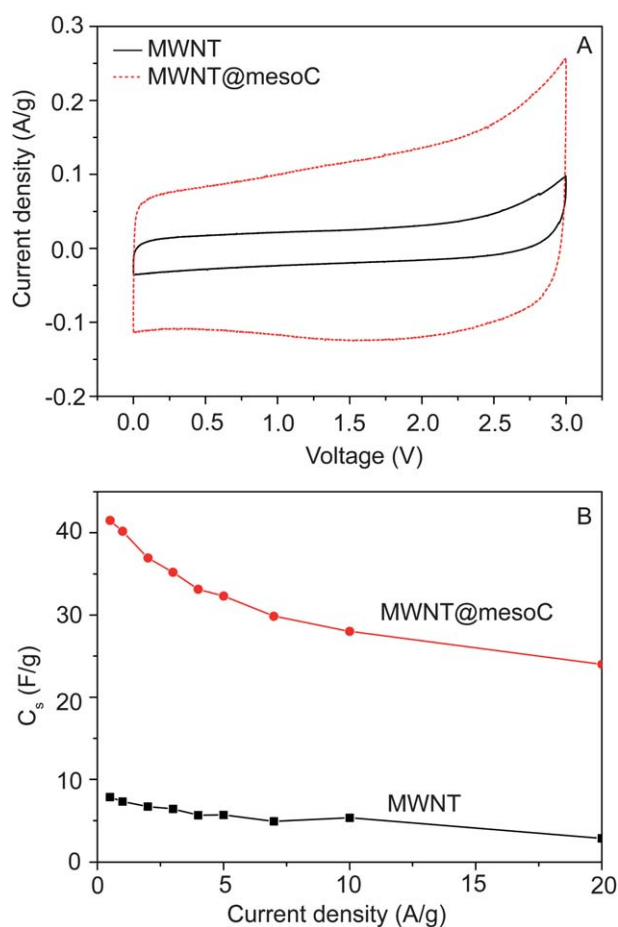


Fig. 6 Cyclic voltammograms at a scan rate of 5 mV s^{-1} (A) and the specific capacitance as a function of current density (B) of the pristine MWNTs and MWNT@mesoC electrode materials in $1.0 \text{ M } (\text{C}_2\text{H}_5)_4\text{NBF}_4/\text{PC}$ electrolyte.

The cyclic voltammogram curves of the pristine MWNTs and MWNT@mesoC composites with core-shell configuration at a scan rate of 5 mV s^{-1} (Fig. 6A) show rectangular shapes and almost negligible current peaks that are probably caused by active oxygen-containing groups, indicating a typical electrochemical double layer behavior. The MWNT@mesoC composite with core-shell configuration has the specific capacitance of 48.4 F g^{-1} , almost fivefold larger than that of the pristine MWNTs (9.0 F g^{-1}), resulting from the increased specific surface areas after the mesoC shell decoration. The rectangular symmetry of the CV curves for the pristine MWNTs and MWNT@mesoC electrodes (Fig. S4, ESI†) is maintained even at a high scan rate of 200 mV s^{-1} , much better than that of the mesoC (Fig. S5a, ESI†). As shown in Fig. 6B, even at a current rate of 20 A g^{-1} , the MWNT@mesoC keeps approximately 60% of the initial capacitance at 0.1 A g^{-1} , indicating the enhanced rate performance relative to the pristine MWNTs ($\sim 37\%$) (Fig. 6B) and mesoC electrodes ($\sim 4.4\%$) (Fig. S5b, ESI†). These results manifest that the 1-D tubular structure and core-shell configuration with short-pore-pathway mesopores as well as 3-D entangled networks allow for easy accessibility of ions to the electrode/electrolyte interface and charging the electrical double capacitors. Cycling performance of the pristine MWNT and MWNT@mesoC electrodes show that nearly 100% and 94% of their initial capacities are maintained after 1000 cycles (Fig. S6, ESI†), indicating apparent superiority of cyclability for the MWNT-based electrodes relative to the amorphous mesoCs ($\sim 60\%$).

The electrochemical performances of the MWNT@mesoC composite were also investigated in 6.0 M KOH (Fig. S7, ESI†). The MWNT@mesoC shows remarkably enhanced specific capacitance (60.2 F g^{-1}) at a sweep rate of 5 mV s^{-1} compared with 6.8 F g^{-1} of the pristine MWNTs, and this C_s value is even close to that of the mesoC (80.5 F g^{-1}) with twofold larger S_{BET} relative to the MWNT@mesoC composite (Fig. S7 and Table S1, ESI†). The result indicates that the increased S_{BET} ($\sim 300 \text{ m}^2 \text{ g}^{-1}$) contributed by the 15 nm thick mesoC shells is highly effective for the formation of EDLC. To evaluate the resistance of the MWNT@mesoC composites relative to the amorphous mesoCs, EIS measurements were performed at -0.35 V vs SCE in 6.0 M KOH . Typical Nyquist plots (Fig. S8, ESI†) display that the diameter of the semicircle in correlation with the charge-transfer resistance of the electrode²⁸ is smaller for the MWNT@mesoC composite (0.10Ω) than that of the mesoC (0.22Ω) in the high-frequency region, which should be attributed to 1-D MWNT inner cores with good electrical conductivity (*i.e.* electron pathway) in the core-shell configuration (Scheme 1a).

The enhanced EC performance for the MWNT@mesoC electrode is in close correlation with its well-designed core-shell configuration. Conductive 1-D MWNT “backbones” with excellent electrical conductivity facilitate the transfer of charges, which can effectively reduce the electrochemical resistance, and thus improve the performance at high operating voltage range. MesoC shells with high specific surface area and short-pore-length ($\sim 15 \text{ nm}$) provide large and effective specific surface areas allowing for easy accessibility of ions to form and charge EDLC at the interface of electrode/electrolyte with low ion-transport resistance. The initial 3-D entangled frameworks of the MWNT@mesoC composites can act as the buffering rooms for the electrolyte to reduce the transport length of ions in the

core-shell configuration. All these proof-of-concept experimental results demonstrate that the well-designed core-shell configuration of MWNT@mesoC composites is effective in application of EC electrodes.

Conclusions

We have designed and synthesized the uniform MWNT@mesoC composites with core-shell structures comprising MWNTs inner cores and mesoC shells by combining a facile sol-gel coating pathway with nanocasting strategy. By using the MWNT@mesoC composite with interpenetrated pores as a hard template, uniform mesoporous carbon shells were successfully decorated on the outer sidewalls of the MWNTs. The obtained composite materials possess evidently increased specific surface areas (from 71 to 381 m² g⁻¹) and uniform bimodal mesopore sizes of 3.9/8.9 nm. EC measurements show greatly increased specific capacitance (from 9.0 to 48.4 F g⁻¹ and 6.8 to 60.2 F g⁻¹ in 1.0 M (C₂H₅)₄NBF₄ and 6.0 M KOH, respectively, compared with that of pristine MWNTs), good rate performance with ~60% maintenance of initial capacitance and excellent cyclability (94% after the 1000 cycles) as well as remarkable electrochemical conductivity. These improved EC performances attribute to the synergistic effect of MWNTs cores with excellent electrochemical conductivity and mesoC shells with relatively high specific-surface-area and short-pore-length (~15 nm). This proof-of-concept study of the correlation between composite-structure and EC performances may provide some reference information for electrode material design and related applications.

Acknowledgements

This work was supported by the NSF of China (20890123), the State Key Basic Research Program of the PRC (2009CB930400, 2009AA033701), Shanghai Leading Academic Discipline Project (B108), and Science & Technology Commission of Shanghai Municipality (08DZ2270500). We greatly appreciate the financial support from Delta Environmental & Educational Foundation (Taiwan).

Notes and references

1 C. Liu, F. Li, L. P. Ma and H. M. Cheng, *Adv. Mater.*, 2010, **22**, E28.

- 2 E. Frackowiak, *Phys. Chem. Chem. Phys.*, 2007, **9**, 1774.
- 3 T. E. Rufford, D. Hulicova-Jurcakova, K. Khosla, Z. H. Zhu and G. Q. Lu, *J. Power Sources*, 2010, **195**, 912.
- 4 P. Simon and Y. Gogotsi, *Nat. Mater.*, 2008, **7**, 845.
- 5 W. Xing, C. C. Huang, S. P. Zhuo, X. Yuan, G. Q. Wang, D. Hulicova-Jurcakova, Z. F. Yan and G. Q. Lu, *Carbon*, 2009, **47**, 1715.
- 6 L. L. Zhang and X. S. Zhao, *Chem. Soc. Rev.*, 2009, **38**, 2520.
- 7 W. Li, F. Zhang, Y. Q. Dou, Z. X. Wu, H. J. Liu, X. F. Qian, D. Gu, Y. Y. Xia, B. Tu and D. Y. Zhao, *Adv. Energy Mater.*, 2011, **1**, DOI: 10.1002/aenm.201000096, n/a.
- 8 E. Frackowiak, K. Metenier, V. Bertagna and F. Beguin, *Appl. Phys. Lett.*, 2000, **77**, 2421.
- 9 A. Izadi-Najafabadi, T. Yamada, D. N. Futaba, M. Yudasaka, H. Takagi, H. Hatori, S. Iijima and K. Hata, *ACS Nano*, 2011, **5**, 811.
- 10 C. G. Liu, M. Liu, F. Li and H. M. Cheng, *Appl. Phys. Lett.*, 2008, **92**, 143108.
- 11 L. L. Zhang, R. Zhou and X. S. Zhao, *J. Mater. Chem.*, 2010, **20**, 5983.
- 12 T. Bordjiba, M. Mohamedi and L. H. Dao, *Adv. Mater.*, 2008, **20**, 815.
- 13 J. Lee, S. Yoon, T. Hyeon, S. M. Oh and K. B. Kim, *Chem. Commun.*, 1999, 2177.
- 14 Q. Li, R. R. Jiang, Y. Q. Dou, Z. X. Wu, T. Huang, D. Feng, J. P. Yang, A. S. Yu and D. Y. Zhao, *Carbon*, 2011, **49**, 1248.
- 15 H. Q. Li, J. Y. Luo, X. F. Zhou, C. Z. Yu and Y. Y. Xia, *J. Electrochem. Soc.*, 2007, **154**, A731.
- 16 D. W. Wang, F. Li, M. Liu, G. Q. Lu and H. M. Cheng, *J. Phys. Chem. C*, 2008, **112**, 9950.
- 17 D. Pech, M. Brunet, H. Durou, P. H. Huang, V. Mochalin, Y. Gogotsi, P. L. Taberna and P. Simon, *Nat. Nanotechnol.*, 2010, **5**, 651.
- 18 D. W. Wang, F. Li, M. Liu, G. Q. Lu and H. M. Cheng, *Angew. Chem., Int. Ed.*, 2008, **47**, 373.
- 19 M. Zhang, Y. P. Wu, X. Z. Feng, X. W. He, L. X. Chen and Y. K. Zhang, *J. Mater. Chem.*, 2010, **20**, 5835.
- 20 D. Y. Zhao, J. L. Feng, Q. S. Huo, N. Melosh, G. H. Fredrickson, B. F. Chmelka and G. D. Stucky, *Science*, 1998, **279**, 548.
- 21 A. H. Lu and F. Schuth, *Adv. Mater.*, 2006, **18**, 1793.
- 22 Y. H. Li, J. Ding, J. F. Chen, C. L. Xu, B. Q. Wei, J. Liang and D. H. Wu, *Mater. Res. Bull.*, 2002, **37**, 313.
- 23 A. Kasuya, Y. Sasaki, Y. Saito, K. Tohji and Y. Nishina, *Phys. Rev. Lett.*, 1997, **78**, 4434.
- 24 C. Thomsen and S. Reich, *Phys. Rev. Lett.*, 2000, **85**, 5214.
- 25 A. Galarneau, J. Iapichella, K. Bonhomme, F. D. Renzo, P. Kooyman, O. Terasaki and F. Fajula, *Adv. Funct. Mater.*, 2006, **16**, 1657.
- 26 L. Zhang, W. C. Geng, S. Z. Qiao, H. J. Zheng, G. Q. Lu and Z. F. Yan, *ACS Appl. Mater. Interfaces*, 2010, **2**, 2767.
- 27 J. X. Zhong and G. M. Stocks, *Appl. Phys. Lett.*, 2005, **87**, 133105.
- 28 H. Zhang, G. P. Cao, Z. Y. Wang, Y. S. Yang, Z. J. Shi and Z. N. Gu, *Nano Lett.*, 2008, **8**, 2664.